

#### Available online at website: https://journal.bcrec.id/index.php/bcrec

Bulletin of Chemical Reaction Engineering & Catalysis, 19 (3) 2024, 521-538



Research Article

# Study on the Phosphate Compound Adsorption onto MgO-KOH/Biochar Adsorbent as Binding Agent in Diffusive Gradient in Thin Film (DGT) Technique for Bioavailable Phosphate Detection

#### Indah Permatasari, Asep Saefumillah\*

Department of Chemistry, Faculty of Mathematics and Sciences, University of Indonesia, Pondok Cina, Beji, Depok City, West Java, 16424, Indonesia

Received: 4th July 2024; Revised: 15th October 2024; Accepted: 16th October 2024 Available online: 18th October 2024; Published regularly: October 2024



#### Abstract

Phosphate compounds, particularly bioavailable forms like PO<sub>4</sub>³-, are critical contributors to eutrophication. In this study, MgO-KOH/biochar was used as a binding agent in the Diffusive Gradient in Thin Films (DGT) technique to enhance phosphate detection. The adsorbent was synthesized from biochar derived from palm oil waste, activated with KOH to increase surface area, and combined with MgO for enhanced adsorption efficiency. The adsorption process followed a pseudo-second-order kinetic model, indicating that chemical interactions dominated the adsorption mechanism. Under different pH levels and phosphate concentrations, the material showed a good selectivity for orthophosphate, achieving an adsorption capacity of approximately 100 mg/g. Characterization via FTIR, XRD, and SAA confirmed the successful synthesis of MgO-KOH/biochar and its structural properties, which contributed to its performance. Additionally, the MgO-KOH/biochar DGT device demonstrated better efficiency in adsorbing PO<sub>4</sub>³-compared to conventional ferrihydrite-based DGT systems, positioning it as a highly effective tool for monitoring bioavailable phosphates in aquatic environments.

Copyright © 2024 by Authors, Published by BCREC Publishing Group. This is an open access article under the CC BY-SA License (https://creativecommons.org/licenses/by-sa/4.0).

Keywords: DGT; Bioavailable Phosphate; MgO-KOH/biochar; Empty Fruit Bunches (EFB); Palm Tree

How to Cite: I. Permatasari, A. Saefumillah (2024). Removal of Tetracycline Using Tungsten Disulfide/Graphene Oxide as Photocatalyst: Effect of Light Irradiation and Kinetic Studies. Bulletin of Chemical Reaction Engineering & Catalysis, 19 (3), 521-538 (doi: 10.9767/bcrec.20178)

Permalink/DOI: https://doi.org/10.9767/bcrec.20178
Supporting Information (SI): https://journal.bcrec.id/index.php/bcrec/article/downloadSuppFile/20178/5319

#### 1. Introduction

Phosphate pollution is a critical environmental issue that impairs eutrophication, disrupting aquatic ecosystems by reducing dissolved oxygen and leading to harmful algal blooms. These blooms not only threaten aquatic biodiversity but also negatively affect water quality and ecosystem services [1]. Whilst bioavailable phosphates, such as orthophosphate (PO<sub>4</sub><sup>3-</sup>), are the primary culprits, other forms of phosphates organic and polyphosphates also persist in water bodies but are less efficiently utilized by plants and algae [2,3]. With the increasing concern over phosphate-induced water

pollution, efficient and selective methods for removing different types of phosphates from water are urgently needed.

Among the many approaches explored, adsorption has emerged as a promising technique for phosphate removal, largely due to its costeffectiveness and high efficiency [4]. Magnesium oxide (MgO) has shown potential as an effective phosphate adsorbent due to its strong affinity for phosphate ions. Several studies focus on enhancing phosphate adsorption. The study by Luo *et al.* [5] used MgO as a cost-effective metal oxide (compared to ZrO<sub>2</sub> and La<sub>2</sub>O<sub>3</sub>), showing a moderate relative affinity for phosphate with a maximum adsorption capacity of 121.950 mg/g for MgO-KOH/biochar (MgO-KBC). However, a

Email: asep.saefumillah@sci.ui.ac.id (A.Saefumillah)

<sup>\*</sup> Corresponding Author.

significant limitation of MgO is its tendency to agglomerate, which reduces its available surface area and, consequently, its adsorption efficiency. To address this challenge, recent studies have investigated combining MgO with biochar, a porous carbon material derived from agricultural waste, to enhance the overall surface area and improve the adsorbent's efficiency [5].

Biochar (BC) is considered environmentally friendly new material [5], with low toxicity, affordability, and flexibility. Despite its high specific surface area, BC has low phosphate adsorption affinity [5]. Indonesia is the world's largest palm oil producer, generating approximately 43.24 million tons of Palm Empty Fruit Bunches annually from the palm oil industry. The Palm Empty Fruit Bunches contains 40-43% cellulose, 22-25% hemicellulose, and 19-21% lignin [6]. The high cellulose, lignin, and hemicellulose content make Palm Empty Fruit Bunches a potential source of biochar. Biochar can be produced through thermal and chemical activation. Chemical activation offers several advantages over thermal activation, such as lower activation process temperatures, higher yields, very high specific surface area, and better pore structure. The main drawbacks compared to physical activation are the corrosive nature of the process and the need for washing steps to remove the activating agents used during this chemical process. Many dehydrating and oxidizing agents have been used in various studies to produce activated carbon/biochar, such as (KOH, K<sub>2</sub>CO<sub>3</sub>, NaOH, and Na<sub>2</sub>CO<sub>3</sub>), alkaline earth metal salts (AlCl<sub>3</sub> and ZnCl<sub>2</sub>), some acids (H<sub>3</sub>PO<sub>4</sub> and H<sub>2</sub>SO<sub>4</sub>), and other agents like B(OH)3 and CaCl2. Among the oxidizing agents, the most efficient is potassium hydroxide, which allows the production of activated carbon/biochar with a high specific surface area and well-developed pore structure. KOH is known as a strong base that is toxic. Still, its toxicity decreases when it changes and is recovered after the chemical activation process to carbonate (K<sub>2</sub>CO<sub>3</sub>), which is typically less toxic than KOH [7]. When biochar is activated with potassium hydroxide (KOH), its specific surface area and porosity are further enhanced, making it an ideal candidate for adsorption applications [5] [8].

Whilst MgO-biochar composites have improved phosphate adsorption, most studies have focused primarily on the removal of orthophosphate, with limited attention to the adsorption of other phosphate species such as organic phosphates and polyphosphates [4]. Moreover, the Diffusive Gradient in Thin Films (DGT) technique, a tool for passive sampling in environmental research, has been underutilized for addressing the selective adsorption of various phosphate species [9]. The effectiveness of DGT devices centres on the binding agent used in the

gel layer, which influences the device's ability to selectively adsorb target analytes during immersion [10]. Whilst MgO has been previously explored as a binding agent in DGT for phosphate removal, it has not been fully optimized for selective adsorption of different phosphate species in complex aquatic environments.

This study aims to demonstrate the role of MgO-KBC, from Oil Palm Empty Fruit Bunches (OPEFB) as carbon source, for binding agent in the DGT device to measure the bioavailability of phosphates. The novelty of this research lies in utilizing MgO-KBC in the DGT technique to not only measure bioavailable phosphate (PO<sub>4</sub><sup>3</sup>-) but also explore its ability to adsorb other types of phosphates, which have received less attention in previous studies. By testing the selectivity of the DGT device with MgO-KBC, we aim to ensure that it can effectively distinguish and capture specific phosphate species, thus contributing to aquatic biodiversity conservation. Furthermore, this study will investigate key factors influencing interaction between MgO-KBC phosphates, such as solution pH, contact time, and phosphate concentration.

#### 2. Materials and Methods

#### 2.1 Materials

The solution of potassium persulfate 50 g.L<sup>-1</sup> was prepared by dissolving 0.5 g K<sub>2</sub>S<sub>2</sub>O<sub>8</sub> (Merck, ≥ 99.0%) in 10 mL distilled water and stored away from light exposure at room temperature. Ascorbic acid (Merck) solution of 100 g.L-1 was prepared fresh daily. The mixed reagent solution was prepared by mixing 30 mL H<sub>2</sub>SO<sub>4</sub> (Merck, 95 98%) (1:1, H<sub>2</sub>O:H<sub>2</sub>SO<sub>4</sub>), 10 mL of 130 g.L<sup>-1</sup>  $(NH_4)Mo_7O_{24}.4H_2O$  (Merck,  $\geq 99.0\%$ ) solution, and 10 mL of 3.5 g.L-1  $C_8H_4K_2O_{12}Sb_2.xH_2O$  (Merck, ≥ 99.0%). The solution was stored at 4oC and stable under these conditions for several months. A phosphate stock solution of 500 mg P/L was prepared by dissolving pre-dried potassium dihydrogen phosphate (KH<sub>2</sub>PO<sub>4</sub>, Merck, ≥ 99.0%) in distilled water. Organic phosphate stock solution of 500 mg P/L was prepared by dissolving Phytic acid (C<sub>6</sub>H<sub>18</sub>O<sub>24</sub>P<sub>6</sup> • xNa<sup>+</sup> • yH<sub>2</sub>O, Merck,  $\geq$ </sub> 90.0% phosphorus basis) in distilled water and stored at 4 °C. A polyphosphate stock solution of 500 mg P/L was prepared by dissolving Sodium Tripolyphosphate (Na<sub>5</sub>P<sub>3</sub>O<sub>10</sub>, Merck, 85%) in distilled water and stored at 4 °C. K<sub>2</sub>S<sub>2</sub>O<sub>8</sub> (Merck,  $\geq$  99.0%) 50 mg/L used for organic phosphate and polyphosphate digestion.

Preparation of Gel Solution using the method by Zhang *et al.* [11]. The polyacrylamide gel consists of 40% acrylamide (Merck,  $\geq$  99.0%) and 0.3% cross-linker N,N'-methylenebisacrylamide (MBA, Merck, 99%) and is used as the diffusive gel layer. In a 10 mL beaker, mix 0.75 mL of MBA, 1,9

mL of 40% acrylamide, and 2.35 mL of distilled water and stirred until homogeneous by using 5 mL of the gel solution for each diffusive and binding gel synthesis.

#### 2.2. Synthesis MgO-BC and MgO-KBC

Five grams of finely ground empty palm fruit bunches (passing through a 40-mesh sieve) were added to 100 mL of KOH (Merck,  $\geq 85.0\%$ ). The mixture was homogenized with a magnetic stirrer for 5 hours. This mixture is referred to as KBC in the future. An amount of 5.5 grams of KBC was added to 1.6 grams of Mg(OH)2, which was made using 100 mL of 2 M Mg(NO<sub>3</sub>)<sub>2</sub> (Merck, 99.0%), 400 mL of absolute ethanol (Merck,  $\geq 99.5\%$ ), and 300 mL of 0.4 M NaOH (Merck, ≥ 97.0%), added slowly. The solution was filtered, and the residue was dried in an oven. The Mg(OH)2 and KBC mixture was stirred with a magnetic stirrer for 24 hours. The solution was dried at 100 °C using an oven. The dry powder was calcined using nitrogen gas at 600 °C for 2 hours, and the powder (MgO-KBC) was washed several times with distilled water. Finally, it was dried in an oven at 80 °C. The base-inactivated biochar was synthesized using the same procedure without the addition of KOH and is referred to as MgO-BC in the future.

#### 2.3. Materials Characterizations

Scanning Electron Microscopy (SEM) coupled with Energy Dispersive X-ray (EDX) (ZEISS, EVO MA 10), X-ray Diffraction (XRD, Malvern PANalytical AERIS), Brunauer-Emmett-Teller (BET, Quadrasorb Evo) method to determine specific surface area, and Fourier Transform Spectroscopy (FTIR, SHIMADZU Infrared IRPrestige-21) was used to materials characterization.

# 2.4. Adsorption Study of MgO, Biochar, and Composites for Phosphate Removal

The study explored the adsorption capacities of MgO, BC, KBC, MgO-BC, and MgO-KBC for phosphate removal. In Erlenmeyer flasks, 50 mL of phosphate solution (10 mg/L) was mixed with 0.050 grams of each adsorbent. The reactions were initiated at room temperature with agitation at 145 rpm. The impact of pH on phosphate adsorption and the maximum adsorption capacity was assessed. Phosphate solutions with varying initial concentrations and pH levels were prepared. The maximum adsorption time was also studied, ranging from 15 minutes to 24 hours. The mixed solutions were filtered using 0.45  $\mu m$  filter paper for subsequent analysis.

#### 2.5. Phosphate Analysis

Three types of phosphates are used in this study: orthophosphate, phytic acid (organic phosphate), and sodium tripolyphosphate (polyphosphate). Phytic acid (PA) and Sodium tripolyphosphate (STPP) solutions require pretreatment before analysis. 70  $\mu L$  of  $K_2S_2O_8$  50 mg/L is added to 10 mL of test solution containing PA or STPP. The solution is heated in a water boiler at 95 °C for 3 hours. After the solution is allowed to cool to room temperature, an analysis is conducted similar to that of the orthophosphate solution.

The analysis is performed by adding a drop of Phenolphthalein to the test solution. If the solution turns pink, add 5 N H<sub>2</sub>SO<sub>4</sub> until the pink color disappears. If the solution remains colorless, add 0.5 mL of Ascorbic acid 100 mg/L and 1 mL of Ammonium molybdate reagent prepared by mixing 100 mL of 130 g/L (NH<sub>4</sub>)Mo<sub>7</sub>O<sub>24</sub>.4H<sub>2</sub>O solution, 100 mL of 3.5 g/L potassium antimony tartrate, and 300 mL of diluted H<sub>2</sub>SO<sub>4</sub> 4N. The phosphate concentration of the samples was analyzed using ultraviolet and visible spectrophotometry (SHIMADZU UV-2400PC Series) molybdenum blue spectrophotometric method [12].

# 2.6. Diffusive Gel in Thin Film (DGT) Preparation

Preparation of Diffusive Gel using the method by Zhang et al. [10]. A total of 35  $\mu$ L of 10% (w/v) ammonium persulfate was added to 5 mL of the previously prepared gel solution and stirred until Then, 12.5μL of n,n,n,nhomogeneous. tetramethyl ethylenediamine (TEMED) added to the solution and stirred for 10 seconds until it became homogeneous. The solution was immediately pipetted into glass molds washed with 0.05 M HNO<sub>3</sub>. The solution was heated in the molds in an oven at  $42 \pm 2$  °C for 1 hour, allowing the gel to form. The formed gel was soaked and hydrated for 24 hours in distilled water, with the water being changed 3-4 times. The diffusive gel was cut to a diameter of 22.5 cm using a DGT cutter and stored in 0.01 M NaNO3 until use. The formed diffusive gel was characterized using FTIR to confirm polymerization.

For the preparation of the MgO binding film, 0.5 g of adsorbent powder was mixed with 5 mL of the gel solution in a 10 mL beaker and stirred until homogeneous. The mixture was placed in an ice bath with ultrasonication for 15 minutes to ensure thorough dispersion of the adsorbent in the gel solution. Subsequently, 35  $\mu L$  of ammonium persulfate and 12.5  $\mu L$  of TEMED were added and stirred for about 10 seconds until homogeneous. The solution was pipetted into glass molds washed with 0.05 M HNO3. The solution in the molds was heated in an oven at  $42 \pm 2$  °C for 1 hour to form

the gel. The formed gel was soaked and hydrated for 24 hours in distilled water, with the water changed 3–4 times. The diffusive gel was cut to a diameter of 22.5 cm and stored in 0.01 M NaNO<sub>3</sub> until use. FTIR was used to characterize the formed diffusive gel for confirmation of polymerization.

During the assembly of the DGT device, the DGT device was washed and rinsed with distilled water, and the filter membrane was soaked in distilled water for 5 minutes. The binding gel was placed first, followed by the diffusive gel and the filter membrane. The DGT device was then closed tightly and securely.

#### 3. Results and Discussion

#### 3.1. MgO-KBC and MgO-BC Synthesis

The synthesis method of MgO-KBC refers to the research by Luo *et al.* [5], which uses the solgel method to synthesize MgO. This method is preferred due to its simplicity, high yield, low reaction temperature, and ability to produce nanoparticles with a small size distribution and large surface area. Ethanol is used to reduce the particle size to the nanoscale and act as a solvent to trigger the nucleation of nanocrystalline particles [13]. This method allows the creation of highly homogeneous composites with high purity (99.99%).

In the sol-gel synthesis, magnesium nitrate precursor Mg(NO<sub>3</sub>)<sub>2</sub> is dissolved in ethanol to form a homogeneous solution. This solution undergoes hydrolysis with water, forming metal hydroxide, which then condenses to form a gel. The gel is dried to achieve nano-size porosity, providing a large specific surface area. This process results in MgO particles with small size distribution and large surface area, enhancing reactivity [14]. Ethanol facilitates the reaction between Mg(NO<sub>3</sub>)<sub>2</sub> and NaOH, producing Mg(OH)<sub>2</sub>. According to Liang *et al.* [15], using Mg(NO<sub>3</sub>)<sub>2</sub> as a precursor significantly impacts MgO-biochar's active sites due to its effect on porosity, structure, and performance as an adsorbent.

The production and activation of biochar occurs in two stages: biochar is mixed with an activating agent and calcined at 600 °C for 2 hours [16]. The calcination process includes four stages: releasing volatile species like CO<sub>2</sub>, NO<sub>x</sub>, and H<sub>2</sub>O due to Mg(OH)<sub>2</sub> and biomass decomposition [15]; etching and combustion between Mg(OH)2 and biomass, creating pores [17]; condensation reactions leading to mass loss; and decomposing Mg(OH)<sub>2</sub> into C-Mg-O at 380 °C, resulting in MgO as the dominant crystalline phase [5]. The yield of the MgO-BC synthesis is 57% of the initial product, which is higher than that of the MgO-KBC synthesis at 43%. This value is similar to the result obtained by Luo et al. [5] in their synthesis of MgO/KBC, which was 41%. The difference in yields between MgO-BC and MgO-KBC can occur because the KOH-activated biochar undergoes faster oxidation at high temperatures. This condition causes the carbon atoms on the surface to oxidize and form pores. This is consistent with the findings of Mestre *et al.* [8], where biomass tends to decompose into powder when activated with alkali hydroxides due to pore formation resulting from the gasification reaction. In other words, the amount of biochar produced is smaller but has a high surface area and porosity.

#### 3.2. Material Characterisations

The morphology and structural characteristics of adsorbents play a crucial role in phosphate adsorption efficiency. Techniques such as Scanning Electron Microscopy (SEM), X-ray Diffraction (XRD), the Brunauer-Emmett-Teller (BET) method, and Fourier Transform Infrared Spectroscopy (FTIR) were employed to analyze and compare the properties of MgO-BC and MgO-KBC. As shown in the Figure 1, the structural differences between these two materials, enlarged at different scales, explain that KOH activation significantly modifies the material's structure. Both the MgO-BC and MgO-KBC samples show irregular, porous structures. The presence of these pores is critical as they increase the surface area available for adsorption. The rough, uneven surface of these biochars provides more sites for interaction, enhancing adsorption capacities. In particular, the MgO-KBC shows a more intricate network, which could imply better performance in trapping smaller contaminants like phosphates.

As shown in Figure 1, the higher magnesium (Mg) content in MgO-KBC compared to MgO-BC can be attributed to the modification process involving potassium (K). In MgO-KBC, potassium plays a significant role in facilitating the deposition and dispersion of MgO onto the biochar surface. This process leads to a more efficient retention of MgO, as potassium promotes better distribution and interaction of MgO with the biochar surface. Potassium's mobility enhances the attaching of MgO, resulting a higher magnesium content in MgO-KBC compared to MgO-BC [18]. It indicates that potassium in biochar modification, increases the reactivity of the surface [19].

MgO-KBC Furthermore, shows fewer impurities, such as silicon (Si), aluminum (Al), and iron (Fe), than MgO-BC. The lower presence of these elements can be linked to the potassium modification process, which likely helps remove inorganic minerals that may otherwise remain on the biochar surface [18]. Studies suggest that potassium can react with impurities like silicates, reducing their presence on the surface and resulting in a cleaner surface with more available MgO-active sites for adsorption [19]. These impurities, particularly silicates and

aluminosilicates, do not contribute to adsorption and may block active sites on MgO-BC, reducing its adsorption efficiency.

MgO-KBC offers more reactive sites for adsorbing phosphorus, which binds effectively with MgO to form magnesium-phosphate complexes [18]. The presence of potassium also contributes to MgO-KBC's performance, as it enhances ion-exchange properties and increases the availability of oxygen-containing functional groups on the biochar surface [18]. These functional groups, along with the finer pore structure observed in MgO-KBC, result in improved adsorption capacity, especially for ionic contaminants like ammonium (NH<sub>4</sub>+) and phosphate (PO<sub>4</sub> $^3$ ) [19].

The FTIR (Fourier Transform Infrared Spectroscopy) spectrum (Figure 2) shows various transmittance peaks for several samples: MgO-KBC, MgO-BC, MgO, Mg(OH)<sub>2</sub>, KBC, and BC. In the BC (Biochar) spectrum, the peak at 883 cm<sup>-1</sup> indicates the presence of C-H bonds, likely from residual organic matter in the biochar. The KBC

(KOH-activated Biochar) spectrum peaks at 582 cm<sup>-1</sup>, indicating an interaction between Mg and O, specifically MgO. In the Mg(OH)<sub>2</sub> spectrum, peaks at 3698 cm<sup>-1</sup> and 3284 cm<sup>-1</sup> indicate the vibrations of Mg-OH bonds and hydroxyl groups (-OH), signifying the presence of Mg(OH)<sub>2</sub> [5].

MgO shows different peaks from Mg(OH)<sub>2</sub>, particularly in the -OH and Mg-OH regions, which are prominent in Mg(OH)<sub>2</sub> but not in MgO, indicating that MgO is purer without hydroxyl groups. In the MgO-BC (Biochar with MgO) spectrum, peaks at 3689 cm<sup>-1</sup> and 3284 cm<sup>-1</sup> indicate interactions between Mg-OH and -OH, and a peak at 1479 cm<sup>-1</sup> indicates C=C bonds within the carbon structure. The MgO-KBC (MgO-KOH activated biochar) spectrum shows a peak at 1662 cm<sup>-1</sup> indicating carbonyl groups (C=O) and a peak at 1479 cm<sup>-1</sup> indicating carbon-carbon double bonds (C=C) [20].

The FTIR spectra of MgO, MgO-BC, MgO-KBC, Mg(OH)<sub>2</sub>, KBC, and BC provide information about the structural and chemical changes that occur during the activation and modification

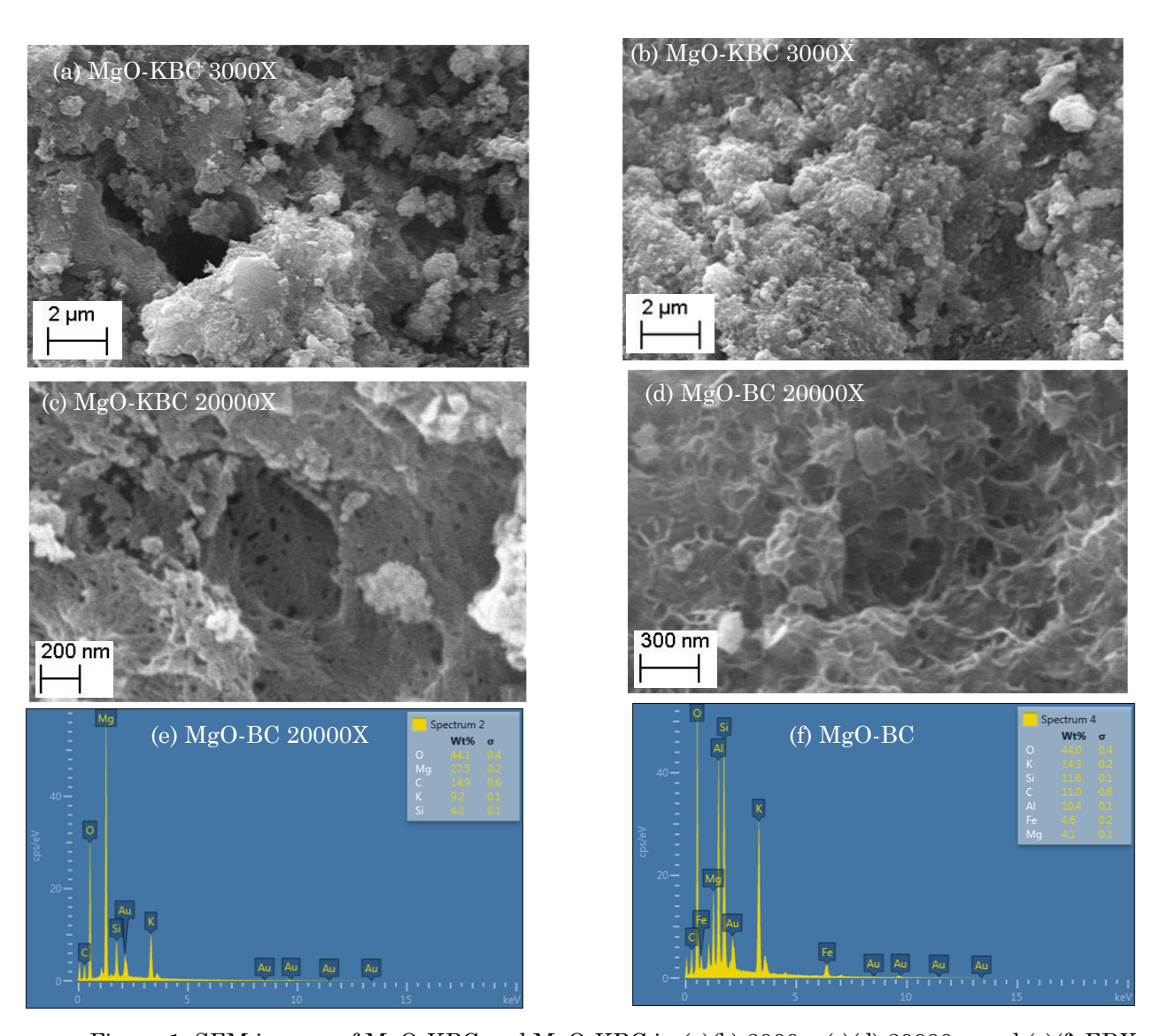


Figure 1. SEM images of MgO-KBC and MgO-KBC in (a)(b) 3000x, (c)(d) 20000x, and (e)(f) EDX

processes. In the MgO-BC spectrum, the peak at 3689 cm<sup>-1</sup> indicates the presence of Mg-OH groups, and the peak at 3284 cm<sup>-1</sup> indicates -OH groups, while the peak at 1479 cm<sup>-1</sup> indicates C=C bonds [21]. The Mg-O peak in MgO (1025 cm<sup>-1</sup>) experiences a slight shift or change in intensity when interacting with biochar, indicating changes in the chemical environment of MgO when integrated with biochar. The MgO-KBC spectrum peaks at 1662 cm<sup>-1</sup> (C=O) and 1479 cm<sup>-1</sup> (C=C), indicating modifications in the KOH-activated biochar structure. Shifts in the dominant Mg-O peak in MgO to different peaks in MgO-KBC indicate changes in vibration frequencies caused by changes in the bond strength between Mg and O when MgO is distributed within the activated biochar structure.

Shifts in FTIR spectrum peaks indicate changes in the chemical environment of specific molecules or ions. In this case, shifts or changes in the intensity of the Mg-O peak when MgO is integrated into biochar suggest changes in bond strength and local structure. Changes in bond strength can occur due to several factors, such as new interactions between MgO and functional groups on biochar, biochar structure modifications, or changes in the oxidation state of Mg. The shift of the Mg-O peak to new peaks in

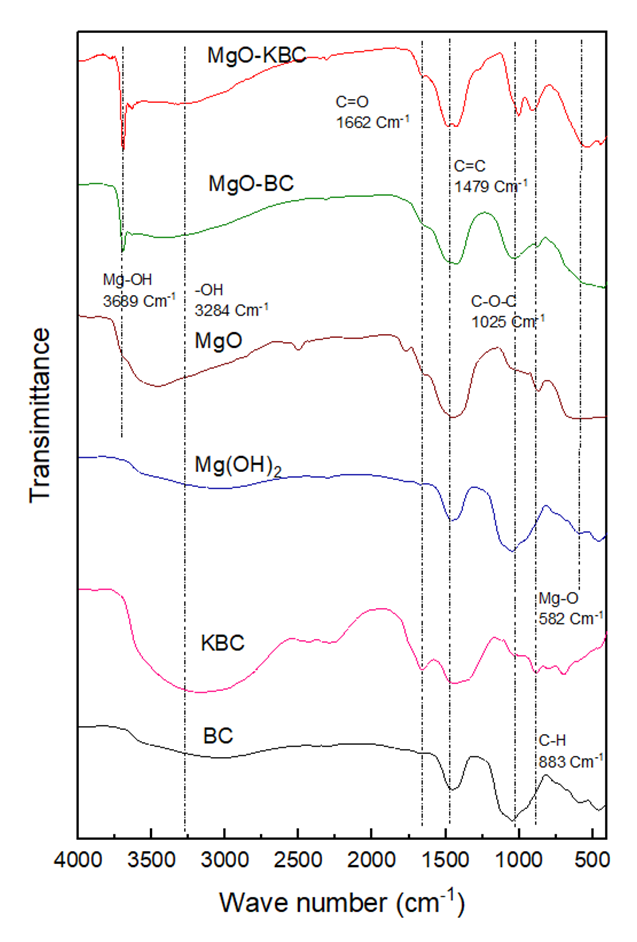


Figure 2 FT-IR spectra of BC, KBC, Mg(OH)<sub>2</sub>, MgO, MgO-BC, and MgO-KBC materials.

MgO-KBC and MgO-BC indicates that the Mg-O bond becomes stronger or weaker depending on the interactions.

Molecular vibration frequencies are sensitive changes in chemical bonds and their surrounding environment. Therefore, changes in vibration frequencies in the FTIR spectrum are an important indicator of the chemical and physical modifications that occur during the activation process and the integration of MgO into biochar. The FTIR spectrum shows that activation and modification of biochar with MgO and KOH result in significant changes in the chemical structure of biochar. The shift of the Mg-O peak in the FTIR spectrum indicates changes in the bond strength between Mg and O caused by new interactions with the carbon structure of biochar. Activation with KOH and integrating MgO create more efficient active sites for adsorption applications, as shown by changes in vibration frequencies in the FTIR spectrum.

The XRD spectra (Figure 3) shows the diffraction patterns of two samples: MgO-KBC and MgO-BC. The crystal structures of Mg<sub>0.06</sub>-O<sub>3</sub> (ICSD01-086-2335), MgO (ICSD00-001-1235), and Mg(OH)<sub>2</sub> (ICSD01-076-0667) are formed in both MgO-KBC and MgO-BC, with labels (a), (b), and (c) respectively indicating the presence of Mg(OH)<sub>2</sub>, MgO, and K<sub>2</sub>CO<sub>3</sub>. For the MgO-KBC sample (red line), there is a peak at around 18° indicating the presence of Mg(OH)<sub>2</sub> (001), dominant peaks at around 37.87°, 42.89°, and 62.06° indicating the presence of MgO (111), (200), and (220), and small peaks around 29° indicating the presence of K<sub>2</sub>CO<sub>3</sub> (label c). For the MgO-BC sample (black line), the main peaks are at around 37.87°, 42.89°, and 62.06° indicating the presence of MgO (label b), and small peaks at around 18° indicating the presence of Mg(OH)<sub>2</sub> (label a) [5].

At a 20 diffraction angle of around 29.44°,

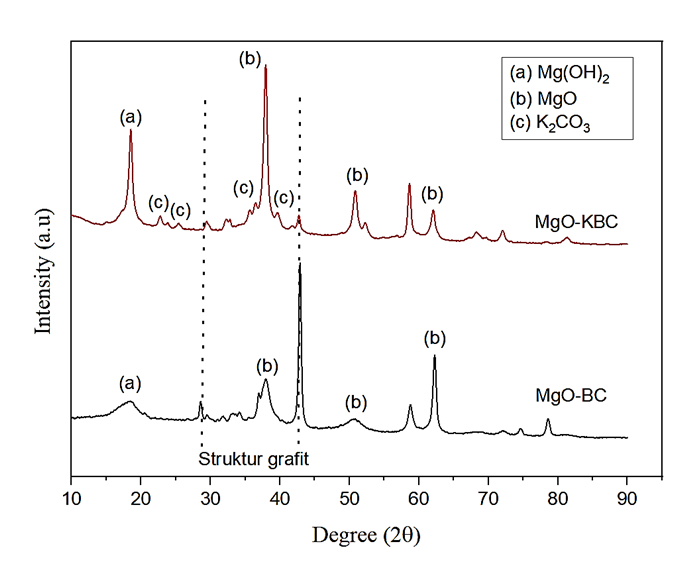


Figure 3 XRD spectra of MgO-BC and MgO-KBC materials.

there is an overlapping structure between the graphite (100) and MgO (200) structures. However, this region has no significant peak, indicating no strong evidence of graphite in the displayed samples. The MgO-KBC sample shows more peaks identified as Mg(OH)<sub>2</sub> and K<sub>2</sub>CO<sub>3</sub> compared to MgO-BC, indicating that MgO-KBC may contain more phases or diverse components. The MgO peaks are more dominant in both samples, indicating that MgO is the main component.

This interpretation is based on the position and intensity of the diffraction peaks compared to the standard database for  $Mg(OH)_2$ , MgO, and  $K_2CO_3$ . The diffraction pattern provides information about the interplanar spacing and crystal symmetry, allowing for identifying components within the sample. Overall, the XRD spectrum indicates that both samples contain MgO as the main component, with a minor presence of  $Mg(OH)_2$  and  $K_2CO_3$ , especially in the MgO-KBC sample.

Using KOH as an activation agent results in an extensive surface area and pore structure, particularly in the micropore region. The isotherms determined for the material with KOH content show the most effective surface and micropore volume development. This observation is confirmed by the structural parameter values in Table 1. Table 1 presents the structural parameter data of MgO-KBC and MgO-BC materials measured using a Surface Area Analyzer. The analysis results show that MgO-

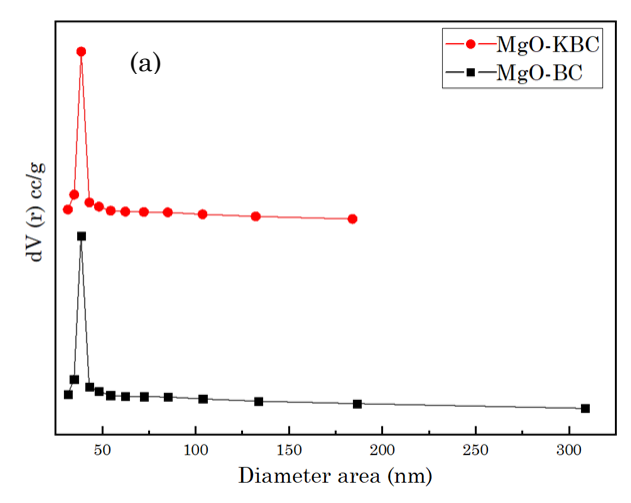
KBC has a significantly larger specific surface area ( $S_{\rm BET}$ ), 272.2153 m²/g, compared to 61.70213 m²/g for MgO-BC. This indicates that MgO-KBC has a more porous structure with more accessible active sites. The external surface area ( $S_{\rm ext}$ ) for MgO-BC is recorded at 52.53033 m²/g, much larger than just 0.005414 m²/g for MgO-KBC. This suggests that most of the surface area of MgO-KBC comes from internal pores.

The micropore surface area ( $S_{\rm micro}$ ) for MgO-KBC is very large, 272.2099 m²/g, compared to only 9.1718 m²/g for MgO-BC. This confirms that most of the surface area of MgO-KBC comes from microscopic pores. The total pore volume (Vtotal) is also larger in MgO-KBC, at 0.31215 cm³/g, compared to 0.115549 cm³/g for MgO-BC, indicating more pore space in its structure. The mesopore volume (Vmeso) of MgO-KBC is 0.311981 cm³/g, larger than 0.108591 cm³/g for MgO-BC, indicating the presence of more or larger mesopores in MgO-KBC.

The micropore volume ( $V_{\rm micro}$ ) in MgO-BC is larger, 0.006958 cm<sup>3</sup>/g, compared to 0.000169 cm<sup>3</sup>/g for MgO-KBC, despite having a larger micropore surface area. This difference may be due to different pore size distributions between the two materials. The pore diameter values are obtained from the pore size distribution graph in Figure 4(a). The much larger pore diameter of MgO-BC, 85.292 nm, indicates that this material has larger mesopores or macropores. Conversely, MgO-KBC has a smaller pore diameter, 2.15 nm, indicating the presence of finer and more uniform

Table 1. Structural parameter data of MgO-KBC and MgO-BC materials obtained by Surface Area Analyzer.

Materials	$S_{BET}$	$S_{\mathrm{ext}}$	Smicro	$V_{\mathrm{total}}$	$V_{\mathrm{meso}}$	$V_{ m micro}$	Pores diameter
	(m <sup>2</sup> /g)	(m <sup>2</sup> /g)	(m <sup>2</sup> /g)	(cm <sup>3</sup> /g)	(cm <sup>3</sup> /g)	(cm <sup>3</sup> /g)	(nm)
MgO-BC	61.70213	52.53033	9.1718	0.115549	0.108591	0.006958	85.292
MgO-KBC	272.2153	0.005414	272.2099	0.31215	0.311981	0.000169	2.15



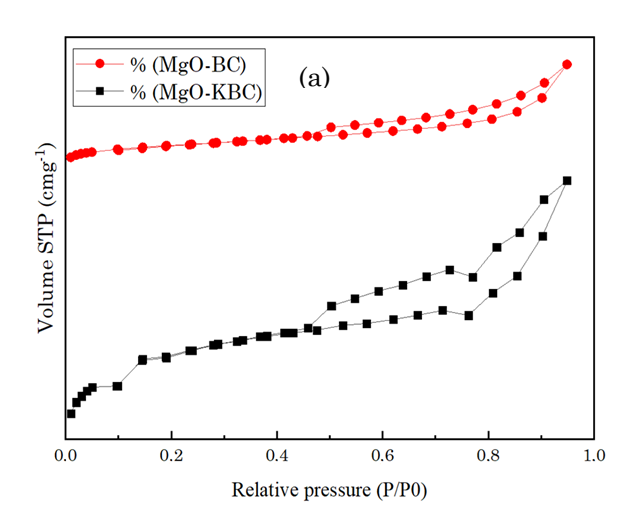


Figure 4 Results of the (a) pore size distribution and (b) adsorption-desorption isotherms measured using a Surface Area Analyzer for MgO-KBC and MgO-BC materials.

micropores. The smaller pore diameter of MgO-KBC corresponds to its very high micropore surface area, resulting from the synthesis process that produces finer and more uniform pore structures.

Figure 4(b) shows the adsorption-desorption isotherms of MgO-KBC and MgO-BC materials, depicting the adsorption capacities of both materials for gases or vapors at various relative pressures. The adsorption isotherm illustrates the relationship between the amount of adsorbate adsorbed on the adsorbent surface and the pressure or concentration of the adsorbate at a constant temperature. In this graph, the X-axis represents the relative pressure (P/P<sub>0</sub>), while the Y-axis shows the volume of gas adsorbed under standard conditions (cm<sup>3</sup>/g). The adsorption curve for MgO-KBC (red) shows a sharp increase in adsorption volume at low relative pressures. It increases significantly to a relative pressure of 1, indicating very high adsorption capacity. In contrast, the curve for MgO-BC (black) shows a slower and lower increase in adsorption volume than MgO-KBC. These results indicate that MgO-KBC has more active sites and a larger pore volume, making it more effective in adsorption.

The type of isotherm shown in this figure is most likely a type IV isotherm according to IUPAC classification [22], indicating the presence of mesopores in the adsorbent material. This is evident from the hysteresis loops between the adsorption and desorption paths, indicating the filling and emptying of mesopores that are not entirely reversible. The hysteresis between both materials' adsorption and desorption paths indicates complex physical and chemical interactions between the adsorbent and adsorbate. Thus, MgO-KBC shows good adsorption performance and is more suitable for applications requiring high adsorption capacity than MgO-BC. The presence of more mesopores and larger pore size in MgO-KBC significantly

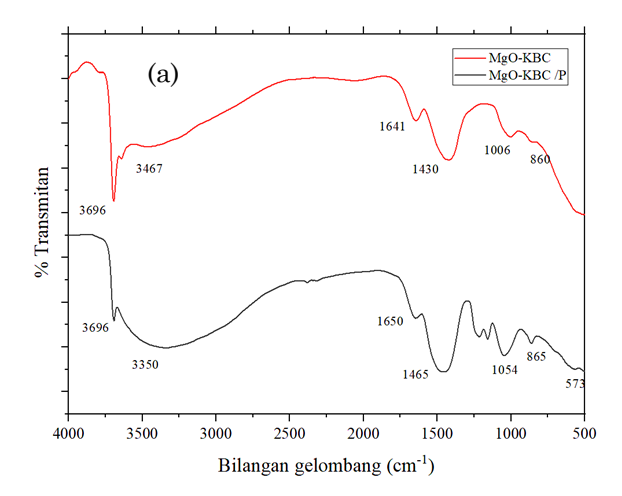
contributes to the increased adsorption capacity and effectiveness as an adsorbent material.

# 3.3. The Effect of Adsorption on Material Characteristics

FTIR is used to analyze the functional groups of materials (MgO-BC and MgO-KBC) that have adsorbed phosphate. As shown in Figure 5, the -OH vibrational group appears at peaks with wavenumbers over 3000 cm<sup>-1</sup>. When comparing the spectra of the initial material and the one that has adsorbed phosphate, there is an increase in intensity at the peaks, indicating the presence of -OH groups. This is due to the protonation of MgO  $(MgO + H_2O \rightarrow MgOH^+)$ . Strong peaks at around 1650 and 573 cm<sup>-1</sup> in the material that has adsorbed phosphate represent MgHPO4 and Mg<sub>3</sub>(PO<sub>4</sub>)<sub>2</sub> bonds, indicating surface complexation between phosphate and biochar. The positive charge of Mg-OH attracts phosphate ions+ through electrostatic attraction.

Additionally, complexation occurs, forming monodentate and bidentate Mg-P surface complexes [15]. Monodentate and bidentate Mg-P refer to the bonding modes between magnesium (Mg) and phosphate (P) on the material surface. One phosphorus atom from the phosphate molecule bonds to one magnesium atom on the surface in monodentate bonding. In bidentate bonding, two oxygen atoms from the phosphate molecule bond to one magnesium atom on the surface.

The FTIR spectrum shown in the graph also compares the material after phosphate adsorption (MgO-KBC/P) and before phosphate adsorption (MgO-KBC). In the MgO-KBC spectrum, significant peaks are observed at 3696 cm<sup>-1</sup> (indicating -OH groups), 3467 cm<sup>-1</sup> (also indicating -OH vibrations), 1641 cm<sup>-1</sup> (indicating C=O bond vibrations), 1430 cm<sup>-1</sup>, and 1006 cm<sup>-1</sup> (indicating C=C and C-O-C bonds). However, after



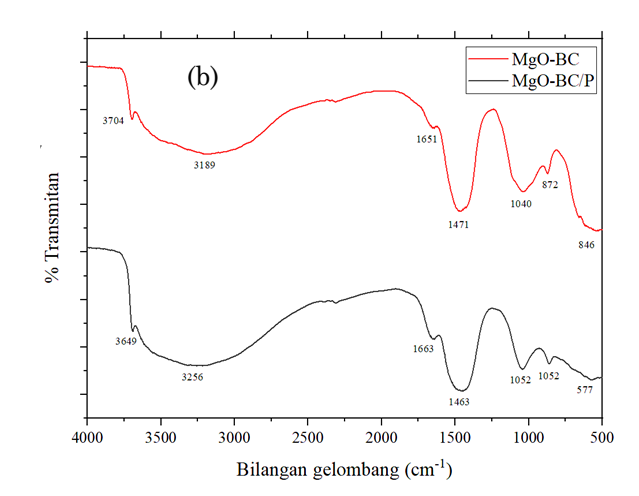


Figure 5. FT-IR spectra of the materials (a) MgO-KBC and (b) MgO-BC, before and after phosphate adsorption.

phosphate adsorption, significant changes occur in this spectrum. The peak at 3467 cm<sup>-1</sup> shifts to a wavenumber of 3350 cm<sup>-1</sup>, indicating that the -OH groups have interacted with phosphate ions. This shift shows that the chemical environment of the -OH groups has changed, causing changes in vibrational energy and frequency (wavenumber). This interaction may involve the formation of hydrogen or covalent bonds between the -OH groups and phosphate ions, making the O-H bonds weaker and longer, thus lowering the vibrational frequency. Therefore, changes in the FTIR spectrum indicate that the -OH groups on the MgO-KBC surface play a key role in phosphate adsorption, involving structural and chemical modifications on the MgO-KBC surface, making it an effective adsorbent for phosphate.

The FTIR spectra of MgO-KBC and MgO-BC significant peaks around 573 cm<sup>-1</sup>, representing Mg-O vibrations. After phosphate adsorption, the spectra of MgO-KBC/P and MgO-BC/P show changes in intensity or peak position shifts. These shifts indicate interactions between phosphate ions and Mg-O sites on the adsorbent surface. Phosphate adsorption causes phosphate ions to bond with magnesium atoms on the MgO-KBC surface, leading to changes in the vibrational energy of the Mg-O bonds. This indicates that the Mg-O active sites on the MgO-KBC surface are highly involved in phosphate adsorption. This interaction may involve the formation of new bonds between phosphate ions and magnesium atoms, altering the Mg-O vibrational frequency and causing changes in the FTIR spectrum. The changes in Mg-O vibrational frequency after phosphate adsorption show that MgO-KBC provides not only physical adsorption sites but also chemical ones. This explains the high efficiency of MgO-KBC in adsorbing phosphate ions from solutions, considering the strong chemical interactions between phosphate ions and magnesium atoms on the adsorbent surface.

According to research by Luo *et al.* [5], the types of bonds between MgO-KBC and phosphate are coordination and hydrogen bonds. The study mentions that the main phosphate adsorption mechanism occurs through the forming of inner-

0.80 MgO-KBC 0.60 MgO-BC 0.40 = -0.0021x + 0.5597·· Linear (MgO-KBC)  $R^2 = 0.8901$ 0.20 Linear (MgO-BC) 0.00 de-dt -0.20 700 500 o -0.40 -0.60 -0.80 -1.00 y = -0.0014x + 0.0249 $R^2 = 0.8028$ 

Figure 6. Adsorption kinetics model of pseudo first order for MgO-KBC and MgO-BC.

time (min)

sphere complexes (coordination) between phosphate and active sites on the MgO-KBC surface, such as Mg-OH and Mg-O. Additionally, hydrogen bonds play a significant role in enhancing phosphate adsorption capacity.

#### 3.4. Adsorption Mechanism

Phosphate adsorption by MgO-BC increases over time, reaching equilibrium at 720 minutes with a residual phosphate concentration of 0.08 g/L, meaning 99% of the phosphate was adsorbed. MgO-KBC also increased over time, reaching equilibrium earlier at 240 minutes. The adsorption capacity of MgO-BC did not change significantly after 88% of the phosphate was adsorbed, indicating high adsorption capacity.

The study examined the effect of initial orthophosphate concentration (0-10 mg/L) on adsorption at room temperature with a 24-hour contact time at pH 5. Adsorption kinetics, essential for understanding the adsorption mechanism of MgO-KBC and MgO-BC, were analyzed using Pseudo first-order and Pseudo second-order models [23]. The pseudo-first-order model assumes that the adsorption rate is proportional to the number of unoccupied active sites on the adsorbent. The linearized form of the pseudo-first-order kinetic equation is expressed as:

$$log(q_e - q_t) = log q_e - \frac{k_1}{2.303}t$$
 (1)

where,  $q_e$  is the amount of phosphate adsorbed at equilibrium (mg/g),  $q_t$  is the amount adsorbed at time t (mg/g),  $k_1$  is the rate constant (1/min), and t is the contact time (min). A plot of log ( $q_e$ - $q_t$ ) versus time should yield a straight line if the system follows pseudo-first-order kinetics. The slope of this line is proportional to the rate constant  $k_1$ .

Figures 6 and 7 showed that the Pseudosecond-order model showed a better result, suggesting that the adsorption process was dominated by chemisorption rather than physisorption [24]. This was evident from the higher correlation coefficients (R<sup>2</sup>) for the pseudo-

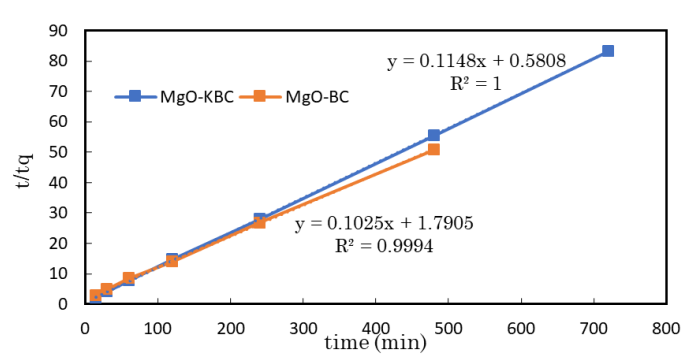


Figure 7. Adsorption kinetics model of pseudo second order for MgO-KBC and MgO-BC.

second-order model and the closer agreement between the experimental and calculated qe values (Table S1, Supporting Information). Therefore, it can be concluded that the adsorption mechanism involves chemical interactions between the phosphate ions and the active sites on the MgO-modified biochar. The pseudo-second-order model is given by:

$$\frac{t}{q_t} = \frac{1}{k_2 q_{e2}} + \frac{t}{q_e} \tag{2}$$

where,  $k_2$  is the rate constant of the pseudo-second-order reaction (g/mg.min).

Adsorption isotherms describe relationship between the amount of a substance adsorbed per unit mass of adsorbent and the concentration of the substance in the liquid phase at equilibrium at a constant temperature. The significance of isotherms in adsorption studies lies in their ability to model and predict adsorption behavior under various conditions. Isotherms help determine maximum adsorption capacity, understand adsorption mechanisms, and optimize adsorption system design for contaminant removal from solutions [25].

Isotherm models are used to see which best fits experimental data. However, not all models must be used if one or a few models sufficiently describe the adsorption process. Choosing the suitable model aids in understanding the adsorption mechanism, optimizing the process, and designing effective adsorption systems. The Langmuir and Freundlich models are used to examine the characteristics of the adsorbent surface. These isotherms are often employed in adsorption studies because of their ability to describe adsorption phenomena with various characteristics [26].

Figure 8(a) shows the Langmuir isotherm plot, where  $C_t/q_e$  is plotted against  $C_t$ . The resulting linear equation is y = 0.0348x + 0.0092 with an  $R^2$  value of 0.9896, indicating that the

data fit well with the Langmuir model. The Langmuir model assumes adsorption occurs on a homogeneous surface with monolayer coverage and no interaction between adsorbed molecules. The R² value close to 1 suggests that MgO-KBC adsorption follows the Langmuir model, indicating monolayer adsorption on a homogeneous surface.

Figure 8(b) shows the Freundlich isotherm plot, where  $\log q_e$  is plotted against  $\log C_t$ . The resulting linear equation is y=0.4447x+3.1742 with an  $R^2$  value of 0.9238, also showing a good fit with the Freundlich model, though not as well as the Langmuir model. The Freundlich model assumes adsorption occurs on a heterogeneous surface with varying adsorption energy, allowing multilayer adsorption. The high  $R^2$  value indicates that the Freundlich model can also explain the adsorption process on MgO-KBC, suggesting a heterogeneous surface and possible multilayer adsorption.

Theoretically, from these two isotherms, it can be concluded that MgO-KBC has surface characteristics that allow for both monolayer and multilayer adsorption, depending on the concentration of the adsorbed substance. The better fit with the Langmuir model suggests the dominance of monolayer adsorption on a homogeneous surface.

#### 3.5. The Effect of pH to Materials Adsorption

pH is a crucial factor affecting the surface charge properties of adsorbents and the form of phosphate in solution [27]. Phosphate adsorption depends on the initial pH of the solution, as shown in Figure 9. Adsorbents with different treatments exhibit different ranges of adsorption capacity. The adsorption capacity of MgO-BC increases from 9.94 at pH = 3 to 9.95 at pH = 7, then decreases at pH of 9 and 12. In contrast, MgO-KBC shows a stable adsorption capacity of around 9.9 from pH of 3 to 7. Both materials show a

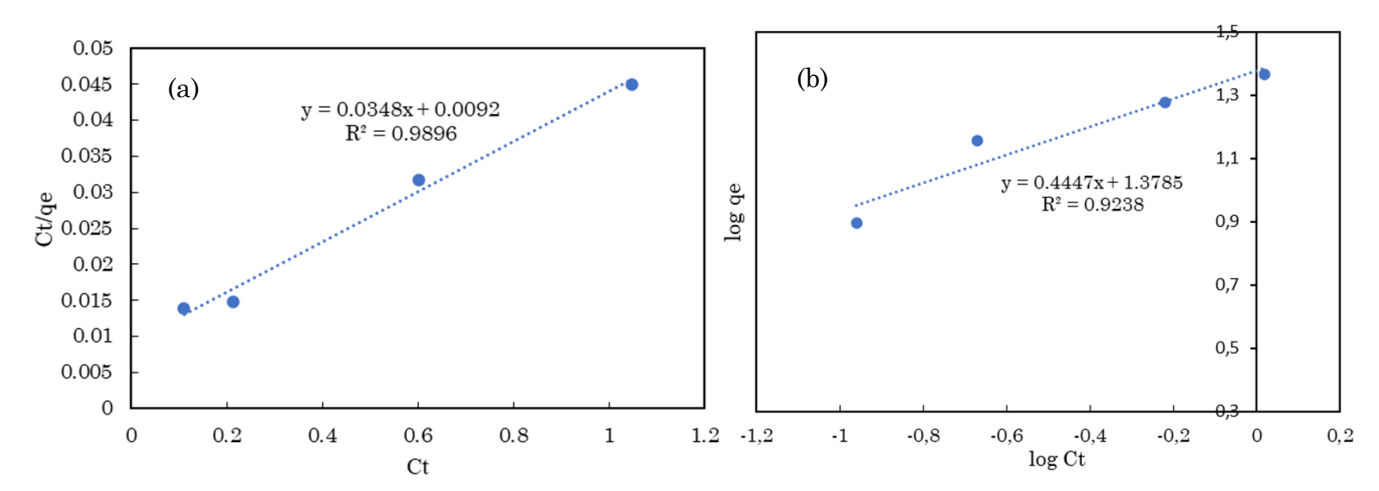


Figure 8. (a) Isoterm Langmuir and (b) Freundlich

decrease in adsorption capacity beyond pH = 7, likely due to competition between phosphate and OH- ions in basic conditions and possible significant deprotonation of the adsorbent surfaces, reducing their affinity for phosphate ions.

The similar adsorption capacities of both materials could be due to their comparable surface areas and site densities, resulting in no significant difference in phosphate affinity [28]. The graph shows that phosphate adsorbed on MgO-BC is higher than MgO-KBC despite the larger surface area of MgO-KBC. This could happen if the phosphate concentration in the solution has yet to reach equilibrium, meaning both adsorbents might not have shown their maximum adsorption capacities. Further research on the effect of pH on phosphate mass adsorption at equilibrium phosphate concentration is needed. Experiments with pH variations aim to examine the effect of initial pH on the adsorption mechanism and the pH of the subsequent solution rather than process optimization. Achieving a pH for maximum adsorption capacity requires pH adjustments, which can increase economic costs [29].

The effect of pH can be explained by the point zero charge (pH<sub>pzc</sub>), surface functional groups of biochar, and phosphate ion species as a function of pH. The pH<sub>pzc</sub> is the pH where the surface charge density of the adsorbent is zero. When the solution pH is lower than the pH<sub>pzc</sub>, the adsorbent surface is predominantly positively charged. Conversely, when the solution pH is higher than the pH<sub>pzc</sub>, the surface is predominantly negatively charged. The Figure S2 (Supporting Information) suggests that the pHpzc for both materials is around 9. Comparing this with phosphate adsorption results, the highest adsorption capacities are observed at pH of 3-7, indicating a positively charged adsorbent surface [30]. This is supported by the statement in the sub-section 3.3

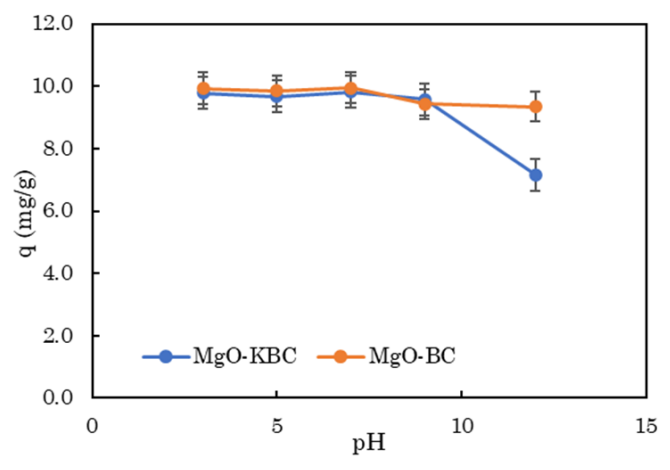


Figure 9. The relationship between pH variation and the adsorption capacity of MgO-KBC for orthophosphate, phytic acid, and sodium tripolyphosphate

which explains that phosphate ions are attracted to the positive charge of MgOH<sup>+</sup> through electrostatic attraction on the adsorbent surface.

3.6. Effects of Concentration, pH, and Contact Time on Adsorption of Different Phosphate Species by MgO-KBC

Figure 10 shows the relationship between phosphate species concentration (PA, OP, and STPP) and MgO-KBC adsorption capacity. It reveals that adsorption capacity increases with phosphate concentrations. concentrations (~2 mg/L), the adsorption capacity for all three phosphates is about 2 mg/g. As the concentration rises to 10 mg/L, the capacity increases, with orthophosphate (OP) reaching nearly 9 mg/g, followed by sodium tripolyphosphate (STPP) and phytic acid (PA).

Many active sites on the MgO-KBC surface are available at low concentrations, allowing efficient adsorption. When phosphate concentrations phosphate increase, more molecules interact with the active sites, enhancing adsorption capacity. Differences in adsorption capacity arise from the distinct adsorption mechanisms of each phosphate. These findings indicate that phosphate adsorption capacity depends significantly on the molecular structure of the phosphates [31]. Further analysis of molecular structure and interaction mechanisms helps explain these differences.

Orthophosphate has a simple structure with one phosphorus atom bonded to four oxygen atoms, allowing easier interaction with MgO-KBC's active sites. Hence, it has a higher adsorption capacity than more complex phosphates. Phytic acid's complex structure, with six phosphate groups attached to an inositol ring, creates more steric hindrance, reducing effective interaction with MgO-KBC. Thus, its adsorption capacity is lower. Sodium tripolyphosphate's linear structure with three phosphate groups also experiences steric hindrance, leading to a lower

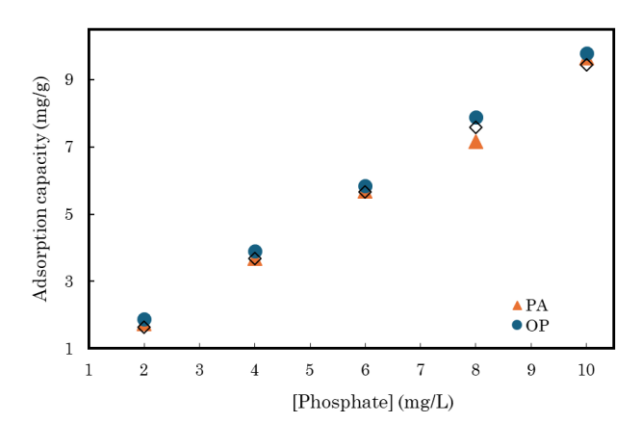


Figure 10. The relationship between phosphate species concentration and the adsorption capacity of MgO-KBC.

adsorption capacity than orthophosphate but potentially higher than phytic acid due to its less complex linear structure.

The adsorption mechanism varies for each phosphate type due to different functional group interactions with MgO-KBC. Orthophosphate likely interacts through direct ionic bonds with MgO active sites, while phytic acid and STPP require specific molecular orientations for effective interaction, hindered by steric and structural complexities.

The effect of pH on the adsorption of various phosphorus (P) types is shown in Figure 11. The adsorption capacity of all three phosphorus types on MgO-KBC is significantly influenced by pH, with the highest adsorption capacity occurring at pH = 5. However, this capacity decreases as pH increases. This decline is due to phosphate's structure or functional groups [32]. According to Yang *et al.* [33], phosphorus is mainly adsorbed through ligand exchange between P and OH<sup>-</sup>. As pH rises, OH<sup>-</sup> ions increase, occupying more active sites on the MgO-KBC surface and competing with P. Additionally, forming a new counterion layer by OH<sup>-</sup> ions inhibits P adsorption [34].

The pH at the point of zero charge (pH<sub>pzc</sub> also plays a crucial role in adsorption [35]. The pHpzc of MgO-KBC is around 9 (Figure S2, Supporting Information), meaning the surface charge of MgO-KBC is positive below this pH. Consequently, at low pH, P adsorption is facilitated by electrostatic and chemical attraction to the positively charged surface. However, when pH rises above the pH<sub>pzc</sub>, the MgO-KBC surface becomes predominantly negatively charged, reducing P adsorption [4]. A study by Luo et al. [5] confirmed the effectiveness of MgO-KBC as a phosphate adsorbent, showing that its unique crystal structure and surface properties enhance its affinity for phosphate through coordination and hydrogen bonding mechanisms. This makes MgO-KBC

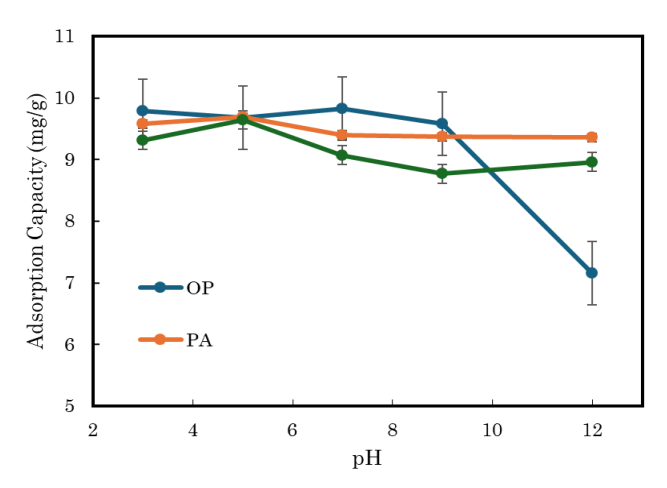


Figure 11. The relationship between ph variation and the adsorption capacity of MgO-KBC for orthophosphate, phytic acid, and sodium tripolyphosphate.

efficient than other adsorbents, especially in lower pH ranges and typical environmental conditions.

The ability of MgO-KBC to adsorb various forms of phosphate such as organic phosphate and polyphosphate over a wide pH range can affect the interaction between the adsorbent orthophosphate in the environment. At lower pH, good to adsorb MgO-KBC has ability orthophosphate and other forms of phosphate, but at higher pH, competition with OH- ions can reduce its effectiveness [36]. In the context of Diffusive Gradient in Thin Films (DGT) applications, the main desired interaction is between adsorbent and bioavailable the phosphate, namely orthophosphate. Significant adsorption of organic phosphate polyphosphate at certain pH levels can interfere with the selectivity towards orthophosphate, which should be prioritized. Therefore, the ability of MgO-KBC to adsorb forms of phosphate other than orthophosphate needs to be considered, especially in its application in DGT devices. The more non-orthophosphate phosphate is adsorbed, can reduce the effectiveness of detecting bioavailable phosphate, which is the main goal in environmental monitoring using DGT technique.

Figure 12 shows the relationship between contact time and the adsorption capacity of MgOphosphates: KBC for three types of orthophosphate (OP), phytic acid (PA), and sodium tripolyphosphate (STPP). The adsorption capacity of MgO-KBC for orthophosphate increases sharply in the first 200 minutes and then stabilizes, reaching a maximum capacity of around 10 mg/g. In contrast, the adsorption capacities for phytic acid and sodium tripolyphosphate remain relatively stable over time, ranging between 8 and 9 mg/g. This indicates that MgO-KBC has a higher affinity for orthophosphate compared to phytic acid and sodium tripolyphosphate.

Theoretically, this aligns with adsorption kinetics principles where, initially, many active sites are available on the adsorbent surface,

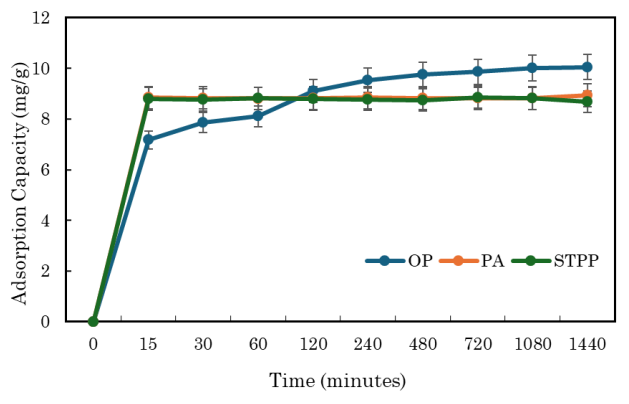


Figure 12. Relationship between contact time and adsorption capacity of MgO-KBC towards orthophosphate, phytic acid, and sodium tripolyphosphate.

allowing rapid adsorption. Once most active sites are occupied, the adsorption rate slows and reaches equilibrium. Orthophosphate, with its simpler molecular structure, can interact more quickly and extensively with the active sites on the MgO-KBC surface. In contrast, the more complex structures of phytic acid and sodium tripolyphosphate have limited access to active sites, resulting in lower and stable adsorption capacities. This demonstrates that the chemical and physical properties of the adsorbent and the molecular structure of the adsorbate significantly affect the adsorption rate and capacity.

## 3.7. Performance of MgO-KBC and Ferrihydrite Binding Gels in DGT Applications for Phosphate Adsorption

The DGT equipment using MgO-KOH/biochar offers several advantages over ferrihvdrite-based systems for phosphate detection. MgO-KOH/biochar, synthesized from palm oil empty fruit bunches (EFBs), not only helps reduce agricultural waste but also enhances phosphate adsorption due to its larger surface area and numerous active adsorption sites. This improved adsorption capacity is reflected in the experimental results, where the concentration of KH<sub>2</sub>PO<sub>4</sub> used ranged from 2 to 10 mg P per L. As a result, the amount of PO<sub>4</sub>3- accumulated by DGT-MgO-KBC and DGT-ferrihydrite (as a commercial product of DGT) increased linearly with the PO<sub>4</sub>3- concentration in the solution (Figure 13). This trend aligns with the theoretically predicted response, and additionally, the CDGT values for MgO-KBC showed a significant increase compared to ferrihydrite. For MgO-KBC gel, the larger surface area and numerous adsorption sites make it more effective as a long-term sampling device.

The graph showing the relationship between the mass of PO<sub>4</sub><sup>3-</sup> accumulated by DGT-MgO-KBC and DGT-ferrihydrite over 24 hours is presented in Figure 14. There is a gradual increase in the accumulated mass of PO<sub>4</sub><sup>3-</sup> over time. According to

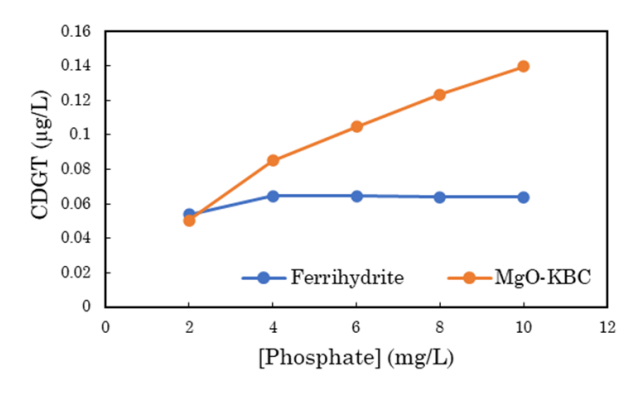


Figure 13. Relationship between  $PO_4^{3-}$  concentration and CDGT in DGT devices using binding agents MgO-KBC and ferrihydrite.

Figure 14, the CDGT values for MgO-KBC are higher than those for ferrihydrite from 1 to 12 hours, peaking at 24 hours for both. This indicates that both DGT devices, with MgO-KBC and ferrihydrite binding gels, require 24 hours for PO<sub>4</sub> accumulation. The recovery rates are 92% for MgO-KBC and over 100% for ferrihydrite. Therefore, a 24-hours immersion time was used for subsequent experiments with DGT on ferrihydrite and MgO-KBC.

pH is an important parameter in aquatic environments, and its influence on DGT devices must be considered to understand its effect on measurement processes. Figure 15 shows the relationship between CDGT and pH. Both materials show a similar pattern at pH of 3, 5, and 7, there are no significant changes, and the trend remains flat. However, changes occur at basic pH levels of 9 and 12. Whilst pH does not significantly affect  $PO_4^{3-}$  accumulation in ferrihydrite, it does in MgO-KBC, especially at basic pH levels. This is consistent with the performance of MgO-KBC, where its  $pH_{pzc}$  value around 9 affects the adsorption process [4].

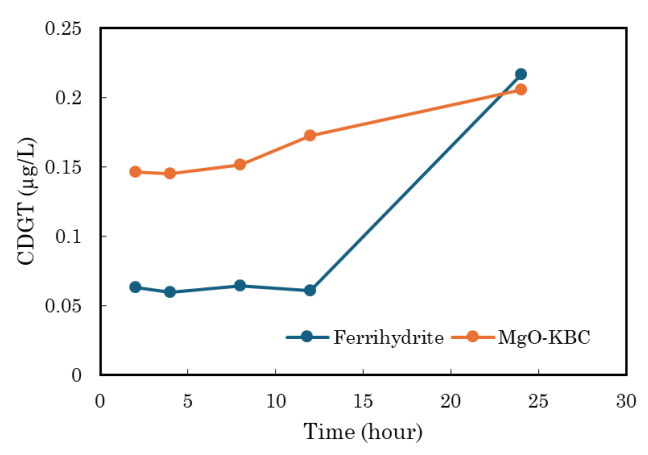


Figure 14. Relationship between contact time of PO<sub>4</sub><sup>3</sup>· and CDGT in DGT devices using binding agents MgO-KBC and ferrihydrite.

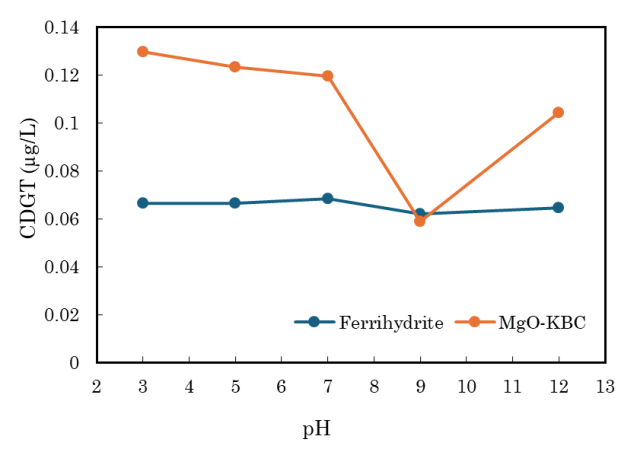


Figure 15. Relationship between pH of PO<sub>4</sub><sup>3</sup>· and CDGT in DGT devices using binding agents MgO-KBC and ferrihydrite.

Based on data presented above, DGT with MgO-KBC achieves equilibrium faster than ferrihydrite, providing quicker and more efficient phosphate accumulation. Additionally, MgO-KBC remains stable across a wider pH range, where ferrihydrite's performance typically declines, making it more versatile in varied aquatic environments. The stronger affinity of MgO-KBC for phosphate ions further enhances its sensitivity, making it a more effective material for environmental monitoring while also promoting sustainable waste management by utilizing agricultural by-products.

Figure 16 shows the relationship between phosphate species (orthophosphate - OP, phytic acid - PA, and sodium tripolyphosphate - STPP) and their concentrations measured using the DGT (Diffusive Gradients in Thin films) technique. DGT is an analytical method used to measure bioavailable species concentrations in solution, often for environmental monitoring. precisely measures bioavailable phosphate, involving diffusion through a gel layer and accumulation on a binding gel. Other anions like and sodium tripolyphosphate acid influence the availability of orthophosphate in the environment. Thus, these anions were added at different initial concentrations (2-10 mg P/L) for the reaction over 24 hours.

The results show that all anions affect phosphate adsorption efficiency by DGT-MgO-KBC. The graph indicates that DGT can detect different phosphate species concentrations at various levels. OP shows the highest CDGT concentration at several points, suggesting that DGT is more sensitive to OP than PA and STPP. This is due to MgO's higher affinity for phosphate ions than the other anions mentioned. Additionally,  $\rm H_2PO_4^{3-}$ , the dominant phosphate ion form in this study, is more readily adsorbed than monovalent anions.

Orthophosphate is the most bioavailable phosphate form in natural and anthropogenic

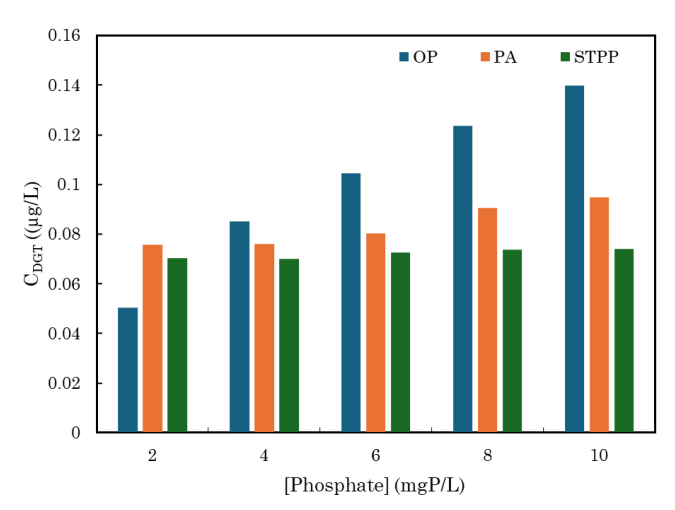


Figure 16. Relationship between phosphate species and CDGT.

biogeochemical processes. PA and STPP are also present in the environment but are less bioavailable than orthophosphate. Ideally, DGT should primarily detect orthophosphate, but the results show PA and STPP can also diffuse into the DGT device, though less than OP. This undesired diffusion may be due to the physical instability of the DGT and binding gels, environmental conditions (like temperature), and detection limits for deficient phosphate concentrations. These factors can selectivity reduce DGT's in phosphate measurement. Further examination of gel pore size is needed to make the device more selective for phosphate species other than orthophosphate.

The selectivity of DGT instruments for different phosphate forms is influenced by several factors. The composition of the binding agent plays a critical role, with materials like ferrihydrite and MgO-KOH/biochar exhibiting different affinities for phosphate species. MgO-KOH/biochar is more selective for orthophosphate due to specific interaction mechanisms, such as inner-sphere complexation [37,38], whereas ferrihydrite can adsorb a broader range of phosphate forms [37]. pH and ionic strength further impact the adsorption process, as the charge of both the binding agent and the phosphate species changes with pH, affecting the of adsorption. MgO-KOH/biochar efficiency remains stable across a wider pH range, enhancing its effectiveness in varying conditions [39]. Additionally, phosphate concentration and molecular structure influence adsorption, with simpler molecules like orthophosphate being more easily adsorbed compared to more complex species like phytic acid, which faces steric hindrance [38,39].

Although the selectivity of MgO-KBC DGT devices requires improvements, their usefulness in adsorbing bioavailable phosphate remains appropriate. In their environmental application, these devices are designed to selectively adsorb and measure phosphates, helping monitor phosphate levels that contribute to environmental concerns such as eutrophication. Moreover, MgO-KOH/biochar offers stability across a wide pH range, making it useful for different aquatic environments. This research suggests that these DGT devices are not only effective for detecting bioavailable phosphates but also provide a sustainable solution by utilizing agricultural byproducts like palm oil waste for biochar production.

In phosphate adsorption studies using adsorbent, the focus is often on key variables like contact time, pH, and concentration because they are easier to control and provide clear insights into the adsorption process. Other factors, such as particle size, temperature, competing ions, and functional groups, also play significant roles but

are often not the primary focus. These variables, however, offer valuable opportunities for further research. For instance, exploring how smaller particle sizes increase surface area or how competing ions in natural water sources reduce adsorption efficiency could deepen the understanding of the process. Investigating these aspects may lead to enhanced materials or methods that improve phosphate adsorption performance in more complex.

#### 3.8. Conclusions

This study successfully demonstrates the enhanced selective phosphate adsorption using a DGT device incorporated with MgO-KOH/biochar (MgO-KBC) synthesized from palm oil empty fruit bunches (EFBs). The research addressed the primary objective by evaluating the performance of the MgO-KBC binding agent in selectively adsorbing bioavailable phosphate species (PO<sub>4</sub><sup>3-</sup>) in comparison to other phosphates. MgO-KBC showed superior selectivity for orthophosphate, achieving better adsorption capacity compared to other phosphate species and outperformed traditional ferrihydrite-based DGT devices.

The study advances the current understanding of selective phosphate adsorption by offering a novel solution that enhances adsorption capacity through the increased surface area and porosity of MgO-KBC. This work contributes to the field by introducing a more efficient method for monitoring and mitigating phosphate pollution in aquatic environments, especially for targeted removal of bioavailable phosphates. The findings provide a strong foundation for further application of MgO-KBC in environmental monitoring devices, with the potential to improve water quality management and remediation efforts.

#### Acknowledgment

We would like to express our sincere gratitude to the Hibah Publikasi Pascasarjana Fakultas Ilmu Pengetahuan Alam dan Matematika University of Indonesia for their financial support (Grant No. PKS-056/UN2.F3.D/PPM.00.02/2024) in the year 2024, which made this research possible. We also extend our appreciation to our advisors for their invaluable guidance and insights throughout the study. Special thanks to the individuals who assisted with proofreading and the technical staff who contributed to the success of this research.

#### **CRediT Author Statement**

Author Contributions: I. Permatasari: Methodology, Formal analysis, Resources, Writing-Original Draft, Visualization, Project administration; A. Sefumillah: Conceptualization, Validation, Investigation, Writing-Review & Editing, Supervision. All authors have read and agreed to the published version of the manuscript.

#### References

- [1] Tirta, A.P., Saefumillah, A., Foliatini, Herawati (2020). The study of phosphate release from artificial sediment into water body using diffusive gradient in thin film (Dgt) device in oxic condition. *Indonesian Journal of Chemistry*, 20(2), 395–403. DOI: 10.22146/ijc.43482.
- [2] Sengupta, S., Pandit, A. (2011). Selective removal of phosphorus from wastewater combined with its recovery as a solid-phase fertilizer. *Water Research*, 45(11), 3318–3330. DOI: 10.1016/j.watres.2011.03.044.
- [3] Egle, L., Rechberger, H., Krampe, J., Zessner, M. (2016). Phosphorus recovery from municipal wastewater: An integrated comparative technological, environmental and economic assessment of P recovery technologies. *Science of The Total Environment*, 571, 522–542. DOI: 10.1016/j.scitotenv.2016.07.019.
- [4] Gao, S., Wang, C., Pei, Y. (2013). Comparison of different phosphate species adsorption by ferric and alum water treatment residuals. *Journal of Environmental Sciences (China)*, 25(5), 986–992. DOI: 10.1016/S1001-0742(12)60113-2.
- [5] Luo, H., Wang, Y., Wen, X., Cheng, S., Li, J., Lin, Q. (2021). Key roles of the crystal structures of MgO-biochar nanocomposites for enhancing phosphate adsorption. Science of the Total Environment, 766 DOI: 10.1016/j.scitotenv.2020.142618.
- [6] Septevani, A.A., Rifathin, A., Sari, A.A., Sampora, Y., Ariani, G.N., Sudiyarmanto, Sondari, D. (2020). Oil palm empty fruit bunchbased nanocellulose as a super-adsorbent for water remediation. *Carbohydrate Polymers*, 229, 115433. DOI: 10.1016/j.carbpol.2019.115433.
- [7] Abbaci, F., Nait-Merzoug, A., Guellati, O., Harat, A., El Haskouri, J., Delhalle, J., Mekhalif, Z., Guerioune, M. (2022). Bio/KOH ratio effect on activated biochar and their dye based wastewater depollution. *Journal of Analytical and Applied Pyrolysis*, 162, 105452. DOI: 10.1016/j.jaap.2022.105452.
- [8] Mestre, A.S., Bexiga, A.S., Proença, M., Andrade, M., Pinto, M.L., Matos, I., Fonseca, I.M., Carvalho, A.P. (2011). Activated carbons from sisal waste by chemical activation with K2CO3: Kinetics of paracetamol and ibuprofen removal from aqueous solution. Bioresource Technology, 102(17), 8253–8260. DOI: 10.1016/j.biortech.2011.06.024.

- [9] Zhang, H., Davison, W. (1999). Diffusional characteristics of hydrogels used in DGT and DET techniques. *Analytica Chimica Acta*, 398, 329–340.
- [10] Zhang, H., Davison, W., Gadi, R., Kobayashi, T. (1998). In situ measurement of dissolved phosphorus in natural waters using DGT. Analytica Chimica Acta, 370, 29–38.
- [11] Zhang, H., Davison, W., Gadi, R., Kobayashi, T. (1998). In situ measurement of dissolved phosphorus in natural waters using DGT. Analytica Chimica Acta, 370, 29–38.
- [12] Worsfold, P.J., Gimbert, L.J., Mankasingh, U., Omaka, O.N., Hanrahan, G., Gardolinski, P.C.F.C., Haygarth, P.M., Turner, B.L., Keith-Roach, M.J., McKelvie, I.D. (2005). Sampling, sample treatment and quality assurance issues for the determination of phosphorus species in natural waters and soils. *Talanta*, 66(2), 273– 293. DOI: 10.1016/j.talanta.2004.09.006.
- [13] Chauhan, A., Shrivastav, A.K., Oudhia, A. (2022). The impact of excessive ethanol on synthesis and characterization of Zinc oxide nanoparticles. *Journal of Crystal Growth*, 591 DOI: 10.1016/j.jcrysgro.2022.126718.
- [14] Bokov, D., Turki Jalil, A., Chupradit, S., Suksatan, W., Javed Ansari, M., Shewael, I.H., Valiev, G.H., Kianfar, E. (2021). Nanomaterial by Sol-Gel Method: Synthesis and Application. Advances in Materials Science and Engineering, 2021 DOI: 10.1155/2021/5102014.
- [15] Liang, H., Wang, W., Liu, H., Deng, X., Zhang, D., Zou, Y., Ruan, X. (2023). Porous MgO-modified biochar adsorbents fabricated by the activation of Mg(NO3)2 for phosphate removal: Synergistic enhancement of porosity and active sites. *Chemosphere*, 324 DOI: 10.1016/j.chemosphere.2023.138320.
- [16] Jamil, U., Zeeshan, M., Khan, S.R., Saeed, S. (2023). Synthesis and two-step KOH based activation of porous biochar of wheat straw and waste tire for adsorptive exclusion of chromium (VI) from aqueous solution; thermodynamic and regeneration study. *Journal of Water Process Engineering*, 53 DOI: 10.1016/j.jwpe.2023.103892.
- [17] Liang, H., Wang, W., Liu, H., Deng, X., Zhang, D., Zou, Y., Ruan, X. (2023). Porous MgO-modified biochar adsorbents fabricated by the activation of Mg(NO3)2 for phosphate removal: Synergistic enhancement of porosity and active sites. *Chemosphere*, 324, 138320. DOI: 10.1016/j.chemosphere.2023.138320.
- [18] Tu, P., Zhang, G., Cen, Y., Huang, B., Li, J., Li, Y., Deng, L., Yuan, H. (2023). Enhanced phosphate adsorption and desorption characteristics of MgO-modified biochars prepared via direct co-pyrolysis of MgO and raw materials. *Bioresources and Bioprocessing*, 10(1), 49. DOI: 10.1186/s40643-023-00670-3.
- [19] Xiao, J., Long, H., He, X., Chen, G., Yuan, T., Liu, Y., Xu, Q. (2024). Synthesis of MgO-Coated Canna Biochar and Its Application in the Treatment of Wastewater Containing Phosphorus. Water (Switzerland), 16(6) DOI: 10.3390/w16060873.

- [20] Xu, S., Li, D., Guo, H., Lu, H., Qiu, M., Yang, J., Shen, F. (2022). Solvent-Free Synthesis of MgO-Modified Biochars for Phosphorus Removal from Wastewater. *International Journal of Environmental Research and Public Health*, 19(13), 7770. DOI: 10.3390/ijerph19137770.
- [21] Zhang, M., Gao, B., Yao, Y., Xue, Y., Inyang, M. (2012). Synthesis of porous MgO-biochar nanocomposites for removal of phosphate and nitrate from aqueous solutions. *Chemical Engineering Journal*, 210, 26–32. DOI: 10.1016/j.cej.2012.08.052.
- [22] Sing, K.S.W., Everett, D.H., Haul, R.A.W., Moscou, L., Pierotti, R.A., Rouquerol, J., Siemieniewska, T. (1985) Reporting Physisorption Data for Gas/Solid System with Special Reference to the Determination of Surface Area and Porosity. *International Union* of Pure and Applied Chemistry, 57(4), 603–619.
- [23] Riahi, K., Chaabane, S., Thayer, B. Ben (2017). A kinetic modeling study of phosphate adsorption onto Phoenix dactylifera L. date palm fibers in batch mode. *Journal of Saudi Chemical Society*, 21, S143–S152. DOI: 10.1016/j.jscs.2013.11.007.
- [24] Xi, H., Zhang, X., Hua Zhang, A., Guo, F., Yang, Y., Lu, Z., Ying, G., Zhang, J. (2022). Concurrent removal of phosphate and ammonium from wastewater for utilization using Mg-doped biochar/bentonite composite beads. Separation and Purification Technology, 285 DOI: 10.1016/j.seppur.2021.120399.
- [25] Lima, É.C., Adebayo, M.A., Machado, F.M. (2015). Kinetic and Equilibrium Models of Adsorption. In: Bergmann, C.P., Machado, F.M. (eds) Carbon Nanomaterials as Adsorbents for Environmental and Biological Applications. Cham: Springer International Publishing, pp. 33–69. DOI: 10.1007/978-3-319-18875-1 3.
- [26] Ye, Y., Jiao, J., Kang, D., Jiang, W., Kang, J., Ngo, H.H., Guo, W., Liu, Y. (2019). The adsorption of phosphate using a magnesia– pullulan composite: Kinetics, equilibrium, and column tests. *Environmental Science and Pollution Research*, 26(13), 13299–13310. DOI: 10.1007/s11356-019-04858-z.
- [27] Wang, H., Zhong, D., Xu, Y., Chang, H., Shen, H., Xu, C., Mou, J., Zhong, N. (2022). Enhanced removal of Cr(VI) from aqueous solution by nano- zero-valent iron supported by KOH activated sludge-based biochar. Colloids and Surfaces A: Physicochemical and Engineering Aspects, 651, 129697. DOI: 10.1016/j.colsurfa.2022.129697.
- [28] Chen, P., Zhou, Y., Xie, Q., Chen, T., Liu, H., Xue, S., Zou, X., Wei, L., Xu, L., Zhang, X., Rosso, K.M. (2022). Phosphate adsorption kinetics and equilibria on natural iron and manganese oxide composites. Journal of Environmental Management, 323 DOI: 10.1016/j.jenvman.2022.116222.

- [29] Pap, S., Gaffney, P.P.J., Bremner, B., Turk Sekulic, M., Maletic, S., Gibb, S.W., Taggart, M.A. (2022). Enhanced phosphate removal and potential recovery from wastewater by thermochemically calcinated shell adsorbents. Science of the Total Environment, 814 DOI: 10.1016/j.scitotenv.2021.152794.
- [30] Borba, L.L., Cuba, R.M.F., Cuba Terán, F.J., Castro, M.N., Mendes, T.A. (2019). Use of adsorbent biochar from pequi (Caryocar Brasiliense) husks for the removal of commercial formulation of glyphosate from aqueous media. Brazilian Archives of Biology and Technology, 62 DOI: 10.1590/1678-4324-2019180450.
- [31] Guan, X.H., Chen, G.H., Shang, C. (2005). Competitive adsorption between orthophosphate and other phosphates on aluminum hydroxide. Soil Science, 170(5), 340–349. DOI: 10.1097/01.ss.0000169908.79614.db.
- [32] Altundogan, H.S., Tumen, F. (2001). Removal of phosphates from aqueous solutions by using bauxite I: Effect of pH on the adsorption of various phosphates. *Journal of Chemical Technology and Biotechnology*, 77(1), 77–85. DOI: 10.1002/jctb.525.
- [33] Yang, Y., Zhao, Y.Q., Babatunde, A.O, Wang L, Ren Y X, Han Y (2006). Characteristics and mechanisms of phosphate adsorption on dewatered alum sludge. Separation and Purification Technology, 51(2), 192–200. DOI: 10.1016/j.seppur.2006.01.01.
- [34] Ye, H.P., Chen, F.Z., Sheng, Y.Q., Sheng, Y.G., Fu, J.M. (2006). Adsorption of phosphate from aqueous solution onto modified palygorskites. *Separation and Purification Technology*, 50(3), 283–290. DOI: 10.1016/j.seppur.2005.12.004.

- [35] Hamdi, N., Srasra, E. (2012). Removal of phosphate ions from aqueous solution using Tunisian clays minerals and synthetic zeolite. *Journal of Environmental Sciences*, 24(4), 617–623. DOI: 10.1016/S1001-0742(11)60791-2.
- [36] Yu, S.H., Feng, X.Y., Fan, M.Y., Zhang, Y.Z., Wang, Y. (2024). Efficient removal of phosphorus and nitrogen from aquatic environment using sepiolite-MgO nanocomposites: preparation, characterization, removal performance, and mechanism. *Environmental Science and Pollution Research*, 31(11), 17481–17493. DOI: 10.1007/s11356-024-32346-6.
- [37] Zhang, C., Ding, S., Xu, D., Tang, Y., Wong, M.H. (2014). Bioavailability assessment of phosphorus and metals in soils and sediments: a review of diffusive gradients in thin films (DGT). Environmental Monitoring and Assessment, 186(11), 7367–7378. DOI: 10.1007/s10661-014-3933-0.
- [38] Zhu, Q., Ji, J., Tang, X., Wang, C., Sun, H. (2023). Bioavailability Assessment of Heavy Metals and Organic Pollutants in Water and Soil Using DGT: A Review. Applied Sciences (Switzerland), 13(17) DOI: 10.3390/app13179760.
- [39] [39] Wu, Z., Wang, S., Zhang, L., Jiao, L. (2016). DGT induced fluxes in sediments model for the simulation of phosphorus process and the assessment of phosphorus release risk. Environmental Science and Pollution Research, 23(14), 14608–14620. DOI: 10.1007/s11356-016-6651-z